Experiments in Fluids (2018) 59:147
https://doi.org/10.1007/s00348-018-2601-5

RESEARCH ARTICLE

# A technique for measuring ensemble-averaged, three-component liquid velocity fields in two-phase, gas–liquid, intermittent pipe flows

**Leonardo S. Fernandes**[1] · **Fabio J. W. A. Martins**[1,2] · **Luis F. A. Azevedo**[1]

Received: 7 June 2018 / Revised: 3 August 2018 / Accepted: 26 August 2018 / Published online: 4 September 2018


## Abstract

Gas–liquid intermittent flows can be found in many engineering applications, nevertheless a detailed knowledge of this flow pattern is still not fully available. In the present work, an experimental study was conducted with the objective of developing a measurement procedure capable of providing ensemble-averaged three-component velocity fields in the liquid phase of a gas–liquid, intermittent, horizontal flow in a pipe. To this end, a high-frequency stereoscopic particle image velocimetry system (SPIV) was employed, combined with the laser induced fluorescence (LIF) technique to separate the light scattered by the liquid–gas interfaces from that emitted by the fluorescent tracer particles. A set of photogates was used to trigger the SPIV system, allowing for the measurement of velocity fields in the liquid plug, downstream of the elongated bubble, and in the liquid film, upstream of the elongated bubble nose position. The triggered measurements allowed the determination of ensemble-averaged three-component velocity fields at different positions in relation to the bubble nose, obtained from the replication of a sufficiently large number of bubble passage events. Contours of the liquid flow streamwise vorticity component in cross-stream planes upstream and downstream of the bubble nose tip were also obtained from the SPIV measurements. The photogate system was also employed to measure the bubble velocity. This information was used to transform time-based into space-based velocity field data. This allowed the construction of a three-dimensional representation of the ensemble-averaged structure of the gas bubble nose and the associated vortical structures induced in the liquid flow. The three-component velocity information obtained revealed the influence of the gas bubble motion on the liquid flow in the plug and liquid film regions.

**Electronic supplementary material** The online version of this article (https://doi.org/10.1007/s00348-018-2601-5) contains supplementary material, which is available to authorized users.

✉ Luis F. A. Azevedo
Lfaa@puc-rio.br

[1] Department of Mechanical Engineering, Pontifical Catholic University of Rio de Janeiro, PUC-Rio, Rio de Janeiro 22451-900, Brazil

[2] Present Address: Laboratory of Fluid Dynamics and Technical Flows, Otto-von-Guericke-Universität Magdeburg, Magdeburg, Germany

**Graphical abstract**

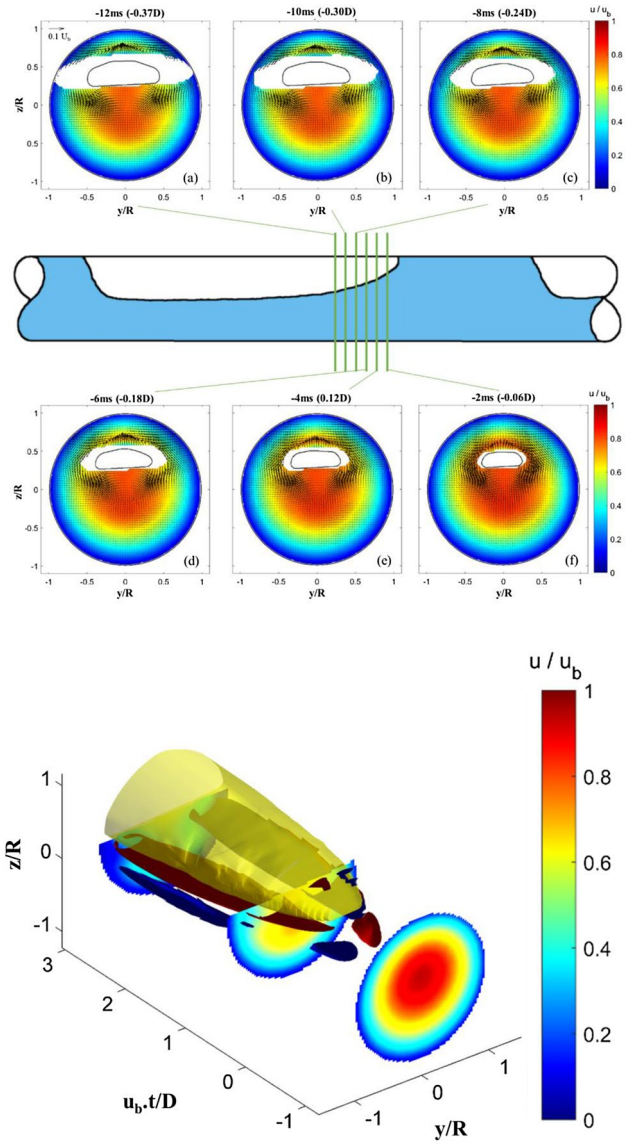


## 1 Introduction

Two-phase, gas–liquid flows in pipes are found in many engineering applications, from petroleum production lines to nuclear cooling systems. When gas and liquid flow simultaneously in a pipe, the type of flow can be classified by the geometric configuration attained by the gas and liquid phases. The intermittent flow configuration, for instance, occurs when the phases are disposed in such a way that gas and liquid flow segregated and in a transient state. For horizontal pipes, shown schematically in Fig. 6, the region where gas flows above the liquid is called liquid film region, and the region where the liquid phase occupies the whole section of the pipe is called liquid plug region. Intermittent flows can be classified into slug flow and elongated bubble flow, depending on the presence of gas bubbles dispersed in the liquid plug (Baker 1954).

Intermittent gas–liquid flows in pipes is a relevant topic of research due to the severe mechanical loads that the transient passage of gas and liquid phases can impose on structures and equipment, having an impact on both its mechanical design and on the process operation (Fabre et al. 1990). Besides the severe problems due to

fluid–structure interactions, intermittent gas–liquid flows are linked to the removal of the anti-corrosion protection coatings on pipe walls, leading to accelerated corrosion (Kvernvold et al. 1984; Carpintero-Rogero 2008).

Modelling of the behaviour of intermittent gas–liquid flows in pipes brings invaluable information to the reliable design and operation of two phase pipe flow systems. The complex nature of such flows, however, precludes the development of precise models without relying on detailed experimental information. In particular, information on the transient velocity fields in the liquid plug and film are relevant to aid in the modelling of pressure drop, heat and mass transfer in intermittent gas–liquid flows. Reliable and detailed experimental information on the velocity field of the flowing phases in two-phase flows has been the focus of intense research for several decades. These are typically difficult measurements to be performed due the transient nature of the flow, and to the complex phase arrangements that prevail in the different flow patterns. The evolution of the measuring techniques along the years, from point measurements techniques (e.g., hot-wire, hot-film, LDV probes) to time-resolved, multi-dimensional techniques has brought invaluable information to help understand the underlying physics governing the flow, leading to better models. In addition, an important role of detailed experimental data is to help validate multi-dimensional numerical simulations of these flows. It is the purpose of the present work to describe an experimental technique capable of producing new information on the velocity field of the liquid phase of intermittent gas liquid flows.

Several authors attempted to measure velocity in intermittent flows. Kvernvold et al. (1984) used the laser Doppler velocimetry (LDV) technique to measure axial velocity profiles in the liquid phase of a slug flow at different positions inside the liquid film and liquid plug. Despite presenting good results, the authors reported problems when performing measurement in aerated regions. Later, Suzanne et al. (1998) concluded that the LDV technique is not feasible for void fractions higher than 2%, due to beam interruption by the dispersed bubbles. Sharma et al. (1998) employed two hot-film anemometers to measure the velocity profile in the axial direction at known positions in the liquid plug and film regions. The hot-film anemometer was also used by Lewis et al. (2002) and Ahmed (2011) to measure the time-averaged axial velocity and void fraction at different positions in the pipe. Both authors agree that, given the transient nature of intermittent flow, there is a large variation in the liquid velocity at different positions along the liquid film and plug. Time-averaged profiles, therefore, might not be a good representation of the physics governing the phenomenon. Bertola (2002) used optical probes to measure the gas–liquid interface velocity profile. The work reported three different velocity profile patterns, depending on the Froude number, that could be used to classify the intermittent flow.

A considerable improvement in this field was made by Carpintero-Rogero (2008), who employed the particle image velocimetry (PIV) technique, along with pulsed shadow technique (PST) and laser induced fluorescence (LIF) to measure the streamwise and transverse vector components of the velocity field in a region close to the bubble nose. The averaged velocity profiles were determined based on only ten instantaneous vector fields, which is considered insufficient to yield converged flow statistics. Carneiro et al. (2011) used the same technique as Carpintero-Rogero (2008), presenting averaged two-component velocity fields based on 150 instantaneous vector fields, which led to better converged statistics. Goharzadeh and Rodgers (2009) employed PIV combined with LIF and refractive index matching to measure the streamwise and transverse components of the velocity in the slug region. An advance on measurements of the velocity field was presented by Czapp et al. (2012), who used the stereoscopic PIV technique (SPIV) to measure all three components of the velocity vector in the liquid phase within a planar cross section of the pipe. However, the velocity profiles presented by Czapp et al. (2012) were based on instantaneous field measurements, what do not represent the stochastic nature of intermittent flows. Siddiqui et al. (2016) used a variation of the classical PIV technique with two cameras mounted with low-pass and band-pass optical filters to measure two-component velocity fields in a slug flow, both in the liquid and gas phases. They measured the streamwise velocity profiles of both phases, revealing its coupled effect. Turbulence information was obtained by means of proper orthogonal decomposition techniques. Recently, Kim et al. (2018) used the PIV technique and capacitance sensors to calculate the flow coefficient based both, on the velocity profiles and on the measured bubble velocity, during intermittent gas–liquid flows. The study was performed with a high viscosity liquid (510, 680 and 960 cP, depending on the temperature) and the authors concluded that the correlation for the flow coefficient proposed by Fabre (1994) might not be valid for laminar elongated bubble flow with low mixture velocities.

Despite the significant improvement observed over the last years in the measurement of the velocity fields associated with intermittent flows, there is still a lack of reliable information in the literature regarding well-converged, averaged three-component velocity fields, in the liquid phase, along the elongated bubble and liquid plug region. The present work describes the implementation of a measuring technique capable of providing reliable information on instantaneous and ensemble-averaged velocity fields of the liquid phase of intermittent gas–liquid flows. As it will be described, the combination of stereoscopic PIV, high frequency lasers, cameras and triggering techniques was able

to provide original information on the three components of the velocity field in the plug and liquid film regions of the intermittent flow.

## 2 Experimental setup

The test section employed in the experiments was designed to allow for the measurement of the three-component vector field in the liquid phase of an intermittent gas–liquid flow, employing the stereoscopic particle image velocimetry (SPIV) and laser induced fluorescence (LIF) techniques. The setup also included optical probes to measure flow statistics and trigger the velocity measurements, as will shortly be described in more details. The experiments were performed for intermittent flow in the elongated bubble regime to facilitate the implementation of the technique, since in this regime fewer gas bubbles are present in the liquid phase, what requires simpler image processing procedures. However, the same technique can be extended for flow regimes where gas bubbles are present in higher concentrations, provided the image processing techniques are properly adapted.

Figure 1 presents a schematic view of the experimental setup. The test section consisted of an 18-m-long, 40-mm internal diameter pipe. The pipe material was acrylic to allow for optical access. A 180° bend, with a radius-to-diameter ratio of 7.5, connected two straight pipe pieces of 193 and 250 pipe diameters in length, as indicated in the figure. The bend was mounted in a horizontal plane, so Fig. 1 is a top view of the installation. The liquid was driven into the test section by means of a progressive cavity pump, while a radial compressor was responsible for the gas supply. Gas and liquid flows entered the pipe through a Y-piece mixer. Elongated bubbles and liquid plugs were hydrodynamically generated due to the imposed gas and liquid superficial velocities and were all formed within the first 20 diameters of the pipe, downstream of the Y-mixer. Calibrated rotameters were used to measure the gas and liquid flow rates. A mixture with 24% of water and 76% of glycerine, in weight, was used as the liquid phase, while air was used as the gas phase. The liquid mixture presented a viscosity of 60.9 cP, density of 1250 kg/m$^3$, refractive index of 1.4368 and a surface tension of 65.70 dyn/cm, all measured at 23 °C. This particular liquid was chosen due to the interest in producing data for intermittent flows with higher viscosity liquids, although any other transparent liquid, such as water, could have been employed. The liquid was kept in a close circuit, returning to the reservoir after passing through the test section, while the air was vented out to the laboratory space. A chiller (not shown in the figure) connected to the liquid reservoir was used to guarantee a uniform temperature for the liquid, ensuring that the liquid viscosity would not change during the experimental campaign. The liquid operating temperature was kept at $23.0 \pm 0.1$ °C. All tests to be reported were conducted with superficial liquid and the gas velocities of 0.4 m/s and 0.2 m/s, respectively, leading to a mixture Reynolds number, $Re_m = \rho_m j_m D/\mu_m$, of 493 and a mixture Froude number, $Fr_m = j_m/\sqrt{gD}$, of 0.96. In the previous definitions, $\rho_m$, $j_m$, and $\mu_m$ are, respectively, the mixture density, superficial velocity and viscosity, while $g$ and $D$ represent the acceleration of gravity and the pipe internal diameter.

The measurement section where the velocity fields were obtained was located 160 pipe diameters downstream of the bend, and at 90 pipe diameters upstream of the pipe ending section. At that position, a visualization box and two high-frame-rate cameras were installed to perform the stereoscopic velocity measurements of the liquid phase. Three

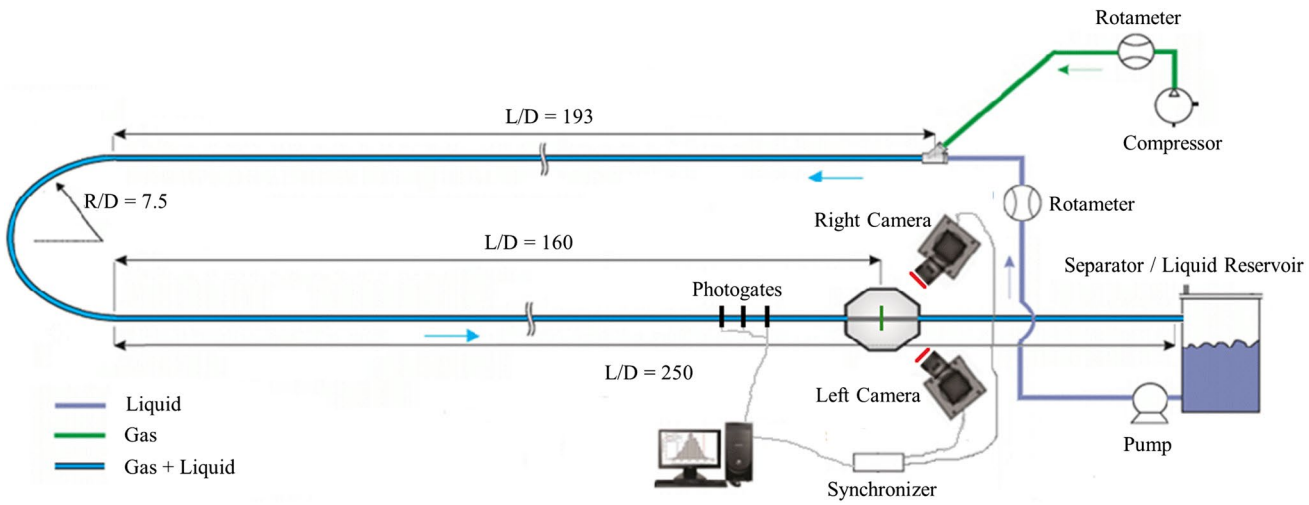


**Fig. 1** Schematic top view of the test section

photogates were placed upstream of the visualization box to allow for the measurements of flow statistics and to trigger the stereo-PIV system, as will be described shortly.

### 2.1 Three component velocity measurements

The three components of the velocity vector of the liquid phase in a pipe cross-sectional plane were measured employing the stereoscopic particle image velocimetry technique. SPIV is a two dimensional, three component technique, capable of measuring the three components of the velocity vector in a plane (3C-2D). Its working principle relies on the processing of tracer particles images, illuminated by a laser light sheet and simultaneously captured from two cameras at different viewing perspectives. The technique uses calibration mapping functions to transform the two-component velocity vectors measured by each one of the two cameras into three-component velocity vectors in the planar measurement region. These mapping functions are usually determined by means of images of a calibration target, which is placed inside the measurement region at the illuminating plane.

The SPIV technique is well established for single-phase flow applications (Prasad 2000; Raffel et al. 2018). However, reflections from the illuminating laser sheet at the gas–liquid interfaces poses limitations on the extension of SPIV to two-phase gas–liquid flows. Indeed, the light reflections at the interfaces are much stronger than the light scattered by the small seeding particles normally used to track the flow. The laser-induced fluorescence technique has been successfully employed in gas–liquid flow measurements as a mean of separating the light scattered from the interfaces from that emitted by the tracer particles (Lindken and Merzkirch 2002; Carneiro et al. 2011; Farias et al. 2012). To this end, fluorescent particles were used as seeding tracers. These particles emit light with a wavelength higher than that of the illuminating laser source. In the present experiments, polystyrene particles impregnated with Rodhamine 6G were employed as tracers. These particles, when excited by the 527-nm wavelength of the laser source, emit light at wavelength of 560 nm. The 24-μm particles had a density of 1.05 g/cm$^3$, and were seeded in the liquid at a concentration of 40 μg/L. High-pass optical filters placed in front of the cameras allowed only the passage of the red light emitted by the tracer particles, blocking the green light scattered by the gas–liquid interfaces. The optical filters are represented by red lines in front of the cameras in Figs. 1 and 2.

Another limiting factor for the application of SPIV to two-phase gas–liquid flows comes from the fact that, in some instances, the presence of gas bubbles precludes the simultaneous view of the tracer particles from the two cameras. This issue will be further addressed in the description of the results obtained in the present experiments.

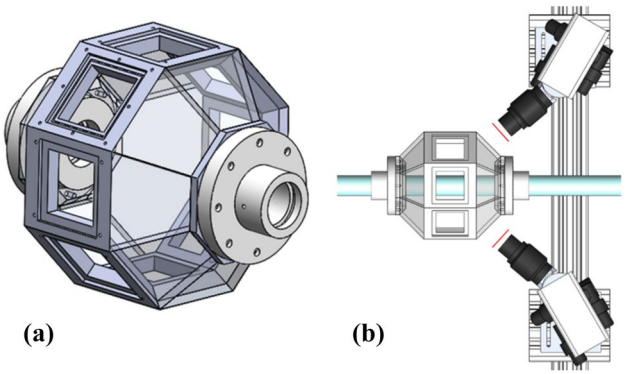


**Fig. 2** **a** Visualization box and **b** stereo PIV camera assembly. Cameras and lens form an appropriate angle to comply with the Scheimpflug's condition (Prasad 2000)

Figure 2 presents a view of the 24-faces visualization box employed in the SPIV measurements with the objective of minimizing optical distortions. The internal space between the box windows and the acrylic pipe mounted through the box was filled with the same water and glycerine mixture used as the working liquid in the tests. The visualization box was designed based on an octagonal shape offering optical access to the fluid flowing in the pipe through 8 flat glass windows and 16 acrylic windows inclined at 45°. This box offers a flexible design that allows the use of multiple cameras and illuminating sources. In the present experiments, only two cameras were employed viewing the flow in the interior of the pipe through two 45° windows, as indicated in the figure. The laser light sheet entered in the box through its bottom plane window, illuminating the cross section of the pipe. To minimize optical distortions associated with the curvature of the acrylic pipe, the length of the pipe that crossed the visualization box had its wall thickness machined down to 1 mm, from its original 5-mm-thick wall. After the machining operation the external surface of the pipe was carefully polished.

Two Phanton Miro M340 cameras were used, both positioned horizontally and with its lenses parallel to the faces of the visualization box, arranged symmetrically at opposite sides of the pipe, as indicated in Fig. 2. The cameras could be operated with a maximum resolution of 1250 × 1200 pixels at a frame rate of 1000 Hz. Micro Nikkor lenses with a focal distance of 105 mm and an aperture of f#11 were used for both cameras, mounted tilted with respect to the camera sensors, to comply with the Scheimpflug's criteria and guarantee uniform focus of the tracer particles in the entire measurement region (Prasad 2000), as seen in Fig. 2. Newport high-pass optical filters with a cut-off wavelength of 550 nm were placed in front of each camera lenses, as required by the LIF technique. A New Wave Nd/YLF Pegasus double-cavity laser (not shown in Fig. 2) were employed as a pulsed

light source. The lasers delivered an energy of 10 mJ/pulse at 1000 Hz. The cylindrical laser beans were shaped into a plane light sheet by combining spherical and cylindrical lenses, which were able to generate a thick plane of about 1.5-mm at the central measurement region. A 45° mirror was used to deviate the light and allow it to come vertically from the bottom of the visualization box, as already mentioned. The cameras and the lasers were synchronized by a TSI 610036 synchroniser, controlled through the Insight 4G software by TSI. Table 1 summarizes the main SPIV parameters used in this work.

### 2.2 Optical probes measuring and triggering system

Three optical probes were installed upstream of the visualization box, as indicated in Fig. 1. The probes were equally spaced 200 mm of each other (5 pipe diameters). They had a dual function of measuring the bubble velocity and triggering the SPIV system for velocity measurements in the liquid phase. The probes were mounted around the acrylic pipe and consisted of beam interrupter devices, or photogates. Each photogate was formed by an infrared red generator and an infrared sensor mounted on opposing sides of the transparent acrylic pipe. The emitted beam reached the opposing sensor depending on the phase present in the pipe. Differences on the index of refraction of the liquid and gas allowed the detection of the phases. When gas was flowing through the probe, the emitted infrared beam reached the sensor producing an electronic signal recorded by the data acquisition system. When liquid was flowing, the beam was deviated and did not reach the sensor. The photogates were positioned in such a way that the infrared beams crossed the upper part of the horizontal pipe, at 2/3 of the pipe diameter. This installation was chosen to take advantage of the fact that the elongated gas bubbles travelled at the upper part of the horizontal pipe, what avoided miss-detection of the elongated bubbles due to the presence of the liquid film in the beam path (de Oliveira et al. 2015). An electronic low-pass filter with a cut-off frequency of 250 Hz was employed to minimize the influence of small dispersed bubbles that produce a high-frequency signal when crossing the infrared beam. The first two upstream photogates were used to measure the bubble nose velocity. The measured transit time of the gas bubble nose between the first and second photogates, together with the known distance between them, yielded the bubble nose velocity information. Bubble velocities were measured in real time. This information was fed to an electronic circuit that waited for the trigger signal of the bubble nose passing through the third photogate, placed 400 mm (10 pipe diameters) upstream of the measurement plane. Once the trigger signal was received, the time necessary for the arrival of the bubble nose at the position of the laser light sheet in the visualization box was calculated by the electronic circuit, and a proper time delay information was sent to the SPIV synchronizer to fire the laser. Once the SPIV system was fired, particle image pairs were captured at 1000 Hz. By varying the magnitude of the time delay sent to the synchronizer, SPIV velocity measurements could be started downstream of the bubble nose position, in the liquid plug region, and proceed into the liquid film region. The information on the bubble translational velocity was also used to transform the time interval between each captured velocity field into space, referred to the nose tip of the elongated bubble. Details of the photogate probes and the logic circuits employed can be found in the work of de Oliveira et al. (2015).

## 3 Stereo PIV image calibration and processing

### 3.1 Image calibration

The camera calibration procedure required for the SPIV technique was performed by means of a calibration rig

**Table 1** Summary of the main parameters for the SPIV technique

| Laser | Nd:YLF 10 mJ/Pulse @1 kHz |
|---|---|
| Camera | Phanton M340 (1250×1200 pixels @ 1 kHz, 10 μm pixel size, 12-bit) |
| Synchronizer | TSI 610036 |
| Camera lens | Focus length: 105 mm, aperture f#11 |
| Processing software | Insight 4G (TSI) and Matlab |
| Seeding | Rhodamine 6G particles ($d_p$ = 24 μm) |
| Spatial resolution | 0.6×0.6 mm |
| Cross-correlation window | 32×32 pixels with 50% overlap |
| Light sheet | Pipe cross section (*YZ* plane), 1.5 mm thickness |
| Valid vectors per field | 3300 |
| Sampling frequency | 1 kHz |
| Acquired particle images | 150 realizations of 400 image pairs per camera (12 Gb/realization) |

specially designed for this experiment. Figure 3a shows a view of the calibration rig. The calibration target was printed on a sheet of polyethylene, in the form of a matrix of 140 equally-spaced points, and glued on a polypropylene disk machined with a diameter slightly smaller than the acrylic pipe internal diameter. The disk was connected to a polypropylene rod that could slide axially through a cylindrical polypropylene sleeve that fitted snugly with the aid of rubber O-rings to the external part of the acrylic pipe. A micrometer head with resolution of 10 μm was connected to the end of the propylene rod, so that the target could be precisely moved axially, as required by the calibration procedure employed. To install the calibration rig into the acrylic pipe section positioned in the visualization box, the acrylic pipe section was disconnected from the main acrylic pipe line. To this end, two sliding coupling located at each side of the pipe piece were displaced. After the introduction of the calibration rig, the opposite end of the pipe was closed and the pipe filled with the same fluid used in the experiments, a mixture of water and glycerine. Figure 3b shows a schematic view of the calibration target placed in the measurement section. It should be mentioned that the visualization box was fixed to supports firmly attached to the laboratory floor. This was necessary to avoid any motion from the calibration target in relation to the cameras during the insertion and removal of the calibration rig. Any relative motion between target and the cameras could invalidate the calibration procedure.

A total of three images of the calibration target in the measurement region, equally spaced of 0.5 mm, were used to create a second-order polynomial mapping for the cameras (Soloff et al. 1997). The micrometer head was used to move the target. A self-calibration procedure was executed after the initial calibration to improve the polynomial accuracy (Bjorkquist 2002; Wieneke 2005).

### 3.2 Image processing

The experiment was designed to capture the velocity vector field at different positions upstream and downstream of the elongated bubble nose tip. To this end, the cameras were positioned downstream of the laser light sheet, as indicated in Fig. 1. Given the nature of the intermittent flow formed by a sequence of air bubbles and liquid plugs, the pipe cross-sectional area occupied by the air varied with time, at the location of the light sheet where the velocity measurements were performed. Upstream of the elongated bubble nose, the air-filled region partially obstructed the images obtained from each camera, producing dark regions, free of particles, at opposite sides of the bubble. In these regions, the reconstruction of the velocity vectors was not possible, since simultaneous images of the particles for the two cameras were not available.

To deal with the limitations caused by this image obstruction, an automatic adaptive masking procedure was developed. The masking procedure separated regions where particles images from both cameras were available, from those regions where images from only one camera was obtained. Figure 4 was prepared to illustrate the automatic masking procedure. The procedure started by acquiring a set of 150 images from each camera, for a fixed time delay. For the case depicted in the figure, a delay of − 10 ms was chosen. The negative sign indicates that the reference bubble nose

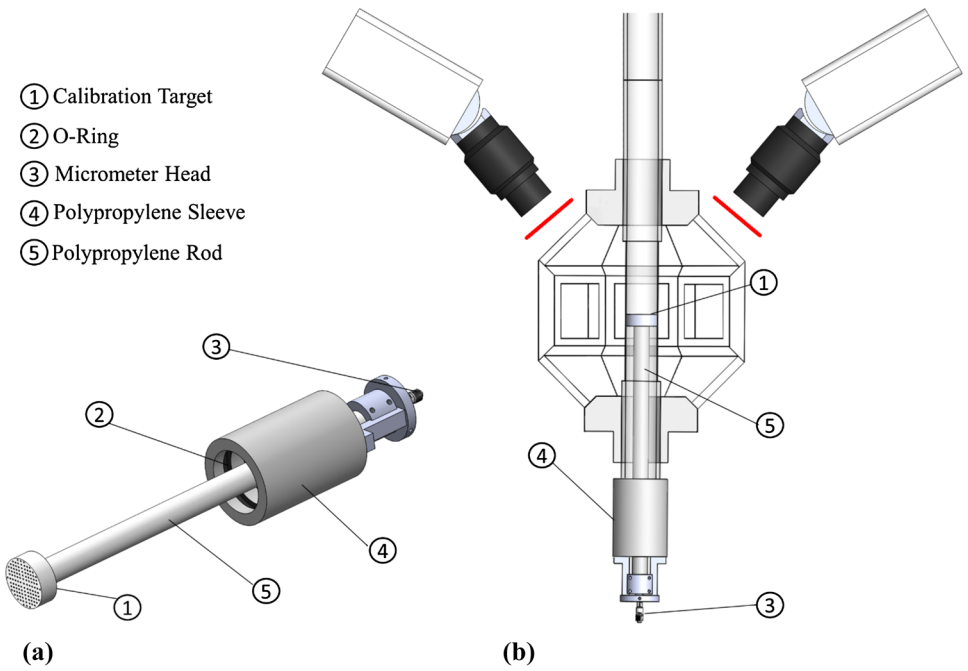


**Fig. 3** Schematic view of the calibration rig employed in the experiments **a** three dimensional view of the calibration rig, **b** top view of the calibration rig mounted in the visualization box. Cameras drawings are not to scale

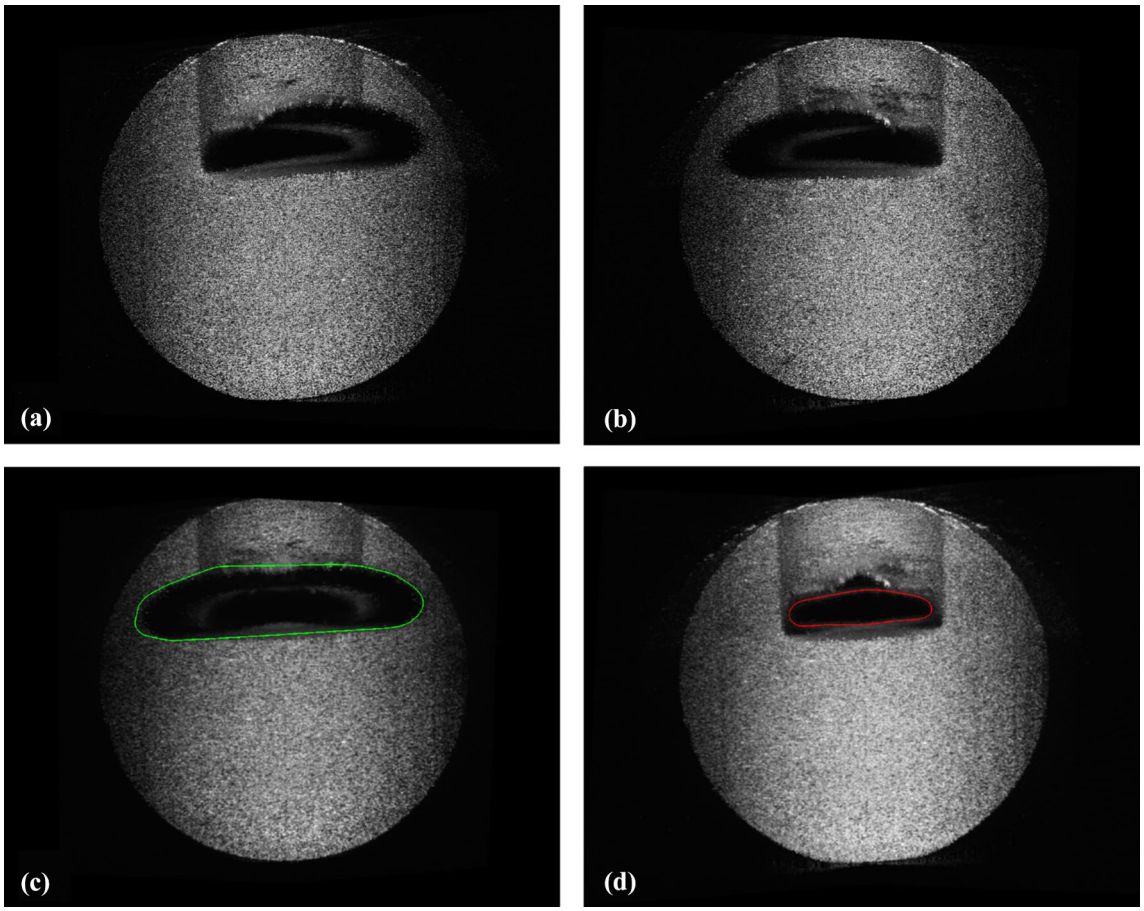


**Fig. 4** Example of results of the image processing procedures employed for masking dark regions and detecting the gas–liquid interface. Image corresponds to a plane captured at 10 ms after the passage of the bubble nose (−10 ms), or situated at 0.3*D* upstream of the elongated bubble nose (−0.3*D*). Maximum intensity image of the 150 acquired and dewarped images at each pixel location for **a** left and **b** right cameras. **c** SPIV mask in green, obtained from the minimum at each pixel location of the maximum intensity image pairs, and **d** detected gas–liquid interface in red, obtained from the maximum at each pixel locations of the maximum intensity image pairs

had already penetrated into the light sheet measuring plane. As already mentioned, this time delay could be transformed into distance from the bubble nose using the measured bubble velocity. In the case of the figure, this time delay would be equivalent to a distance of −0.3*D*, where *D* is the pipe diameter. The acquired 150 pairs of images were dewarped by the polynomial mapping, generated by the calibration procedure already described. A new image was generated for each camera, formed by the binarized maximum intensity of each pixel, in each of the 150 acquired images. Figure 4a, b show the resulting binarized maximum intensity images for the left and right cameras, respectively. The aforementioned dark regions at each side of the bubble are clearly seen.

The mask necessary for computing the velocity field using the SPIV technique was computed by forming an image with the minimum intensity at each pixel of the two binarized maximum intensity images (Fig. 4a, b). The resulting image is shown in Fig. 4c. It should be mentioned that the study of elongated bubble tail regions, which is not the aim of the present work, would require cameras placed upstream of the laser light sheet position, to minimize the size of obstructed regions.

Since no tracer particles are expected to be present in the gas region, the gas–liquid interface contour was obtained by generating an image formed with the maximum intensity at each pixel of the two maximum intensities images from the two cameras, i.e., from Fig. 4a, b. The resulting image is presented in Fig. 4d, where the interface obtained can be observed marked with a red contour. Standard closing and opening binary operations were performed to smooth and close the gas–liquid and mask interfaces. As can be seen, the obstructed region was larger than the gas–liquid interface contour, as expected. The image processing to construct the mask was performed with Matlab software. The somewhat darker rectangular region above the bubble contour is due to attenuation caused by the gas region on the laser light sheet coming from below.

For the data runs, 150 bubble passage realizations were acquired. For each realization, 400 images were acquired at a 1 kHz frame rate, as the bubble crossed the illuminating plane. The acquired images were processed using the software Insight 4G employing a multipass sub-pixel shift cross-correlation. The images were dewarped using the second-order polynomial mapping, to correct for the camera oblique views. The slight reflections at the wall, due to particles deposited on the pipe surface, as well as small non-uniformities on laser illumination, were corrected by subtracting, from each image, the image formed with minimum intensity at each pixel, for each of the 150 images acquired by each camera. The final cross-correlation window on these pre-processed images was $32 \times 32$ pixels, with an overlap of 50%, what led to a grid resolution of $0.6 \times 0.6$ mm for the velocity vectors. With this resolution, each image generated a velocity field with 3300 vectors.

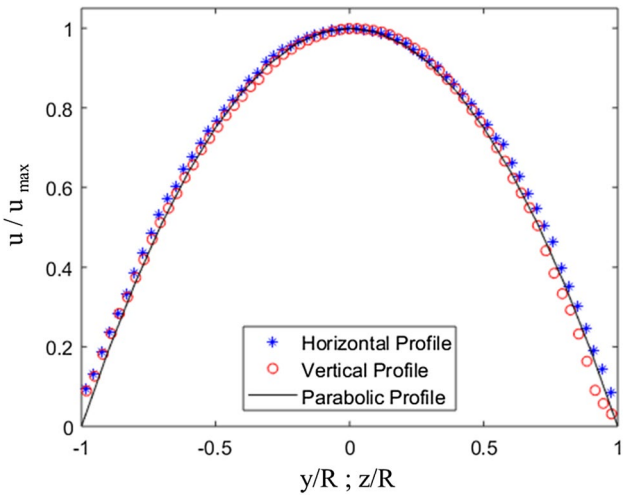


**Fig. 5** Comparison of measured average streamwise horizontal and vertical velocity profiles with the analytic parabolic profile for a hydrodynamic fully developed laminar liquid flow, for $Re = 312$

## 4 Validation experiments

Before performing the intermittent flow experiments, the test section, the experimental procedure and the image processing techniques employed were validated by measuring the velocity profile of a single phase, laminar, fully developed flow. To this end, the test section was operated completely filled with liquid at a flow rate of 0.48 L/s, corresponding to an average velocity of 0.38 m/s, and to a Reynolds number of 312. A total of 350 pairs of particle images were acquired and processed, to yield instantaneous velocity fields that were averaged to yield the average velocity field. Streamwise velocity profiles along the vertical and horizontal axis in the cross-sectional plane are presented in Fig. 5, together with the analytic parabolic profile. The profiles were normalized by the maximum average streamwise velocity, $u_{max}$, of 0.75 m/s, while the radial and transverse coordinates were normalized by the pipe radius $R$, equal to 20 mm. As can be seen in the figure, excellent agreement was obtained between the experimental data and the parabolic profile, for both the horizontal and vertical profiles. The root mean square error between the measured velocity profile and the parabolic regression was below 2% of $u_{max}$. The flow rate obtained by integrating the measured velocity profile deviated less than 3% from the flow rate measured at the liquid-rotameter. This small discrepancy was within the rotameter uncertainty level.

The measured hydrodynamic fully developed laminar flow profile was also used to correct the slight offset of the grid center of the SPIV fields. The grid generated during the calibration procedure used the center of the target as a reference origin for the $Y$ and $Z$ axis. In the present work, $X$ refers to the streamwise direction, while $Y$ and $Z$ are the horizontal and the vertical directions, respectively. Despite all care to guarantee the alignment of the center of the target with the pipe axis, a small offset was expected. The grid origin was corrected using a second-order interpolation function to determine the coordinates of the maximum average streamwise velocity value in the pipe cross section, which would correspond to the center of the pipe. The offset measured was less than 0.5 mm, both in the $Y$ and $Z$ directions.

## 5 Uncertainty on velocity measurements

The uncertainty on the instantaneous velocity fields was estimated based on the root-mean-square fluctuations of the in-plane velocity components for the hydrodynamic fully developed laminar liquid flow results. Due to the symmetric camera arrangement of the present SPIV experiment, the uncertainty in all velocity components are expected to be of the same order. For this uncertainty estimate, it is assumed that the influence of slight flow rate oscillations from the pump and other flow instabilities were negligible on these in-plane components for the laminar liquid flow studied.

The standard uncertainty on the ensemble-averaged velocity field obtained from the 350 instantaneous fields was calculated from the root-mean square fluctuations over both the flow cross sectional area and the instantaneous velocity fields, and contained the random (Type-A) and the systematic (Type-B) uncertainty components. The random component is obtained from the standard deviation divided by the square-root of the number of independent samples used to compute the average. Due to the high number of samples employed, the contribution from the random uncertainty component becomes negligible when compared to the systematic component, so that the combined

standard uncertainty on the average field was estimated as being of the same order as that for the instantaneous field. The computed root-mean square fluctuations over the flow cross sectional area was 0.008 m/s. This value was taken as an estimate for the standard systematic uncertainty of the instantaneous velocity components measurements, what is equivalent 0.05 pixel. This standard systematic uncertainty, refers to a one standard-deviation of the distribution, being associated to a 68% confidence level (BIPM et al. 2008; Sciacchitano and Wieneke 2016).

In the experiments performed, the time intervals between consecutive laser pulses were set to produce similar streamwise particle displacements in pixels for the laminar and intermittent flows. In view of that, the estimates of uncertainty in the instantaneous and average velocity fields obtained from the laminar experiments were employed also for the intermittent flows. It should be recalled that the uncertainty estimates just mentioned are average values calculated over the flow cross section. Local uncertainty values close to the pipe wall or gas–liquid interface are expected to be larger.

## 6 Results and discussion

The average translational velocity of the elongated bubble, measured as described with the photogates, was $U_b = 1.22$ m/s, with a standard deviation of 0.07 m/s. This value was based on 1000 measurements of individual elongated bubbles passing through the measurement sections. As explained, the measured average bubble velocity was used to convert the 1 ms time interval between the acquired image pairs into a distance of $0.03D$. This conversion of time into space will be used along the text, together with the proper time delay after or before the arrival of the elongated bubble at the measurement section. From the measurements with the photogates, statistical information on the elongated bubbles formed was obtained and is presented in Table 2.

The results obtained for the velocity fields in the liquid phase of the horizontal intermittent flow will now be presented. Since the main objective of the study is to describe the technique employed for the velocity measurements, results will be presented for a single combination of superficial gas and liquid velocities, as already mentioned, 0.4 m/s and 0.2 m/s, respectively, corresponding to a mixture velocity of 0.6 m/s, a mixture Reynolds number of 493 and a mixture Froude number of 0.96. Under these flow conditions, the prevailing intermittent flow regime is elongated bubble. This flow regime facilitates the testing of the measuring procedure developed due to the small number of bubbles dispersed in the liquid plug. The measurement of velocity fields in liquid plugs with higher number of dispersed bubbles, characteristic of the slug flow regime, can also be handled by the measuring technique described here with some additional image processing procedures. This is the focus of our current developments, and will not be presented here.

**Table 2** Statistical information on the elongated bubbles

| | Average value | Standard deviation |
|---|---|---|
| Bubble length/diameter | 13.16 | 1.17 |
| Bubble velocity (m/s) | 1.22 | 0.07 |
| Liquid plug length/diameter | 10.05 | 0.98 |

For each of the 150 experimental realizations formed by individual bubble passages, a total of 400 instantaneous velocity fields in the pipe cross-sectional plane were acquired and processed along the liquid plug and film regions, resulting in 400 ensemble-averaged velocity fields. These velocity fields were separated by a time interval of 1 ms, ranging from −200 ms (upstream of the elongated bubble nose, in the liquid film region) to 200 ms (downstream of the bubble nose, in the liquid plug region). The bubble nose tip was used as the reference position for the analyses.

The average three-component velocity fields in the pipe-cross section at different positions in the vicinity of the bubble nose are shown in Fig. 6 for the liquid plug region. Also included in the figure is a sketch of the bubble in the pipe to facilitate the interpretation of the velocity results presented. Each velocity field in the figure is identified, both, with the time delay and axial position in relation to the bubble nose tip. The spanwise components of the velocity are indicated by the black arrows, while the streamwise velocity component is color-coded to the scale in the figure. The magnitudes of the velocity components were normalized by the average bubble nose velocity, $U_b = 1.22$ m/s. A reference vector of magnitude $0.1U_b$ is displayed at the upper left corner of the velocity field of Fig. 6a. The fine spatial resolution achieved with the SPIV measurements implemented in the present work can be observed in the plots.

The vector plots in the cross section planes within the liquid plug downstream of the bubble nose are shown in Fig. 6a–f for streamwise positions ranging from $0.06D$ to $0.37D$. The observation of the measured flow field closest to the bubble nose, $0.06D$ in Fig. 6a, indicates that the liquid is pushed forward and downward, due to the fact that the gas bubble moves faster than the liquid average velocity (Dukler and Hubbard 1975), and occupies the upper part of the pipe cross section. Indeed, a region of strong downward jet-like flow is present along the center part of the pipe cross section. A pair of perfectly symmetric, counter-rotating streamwise vortices is observed siding the downward center jet flow. These recirculation zones are confined to the lower half of the pipe cross

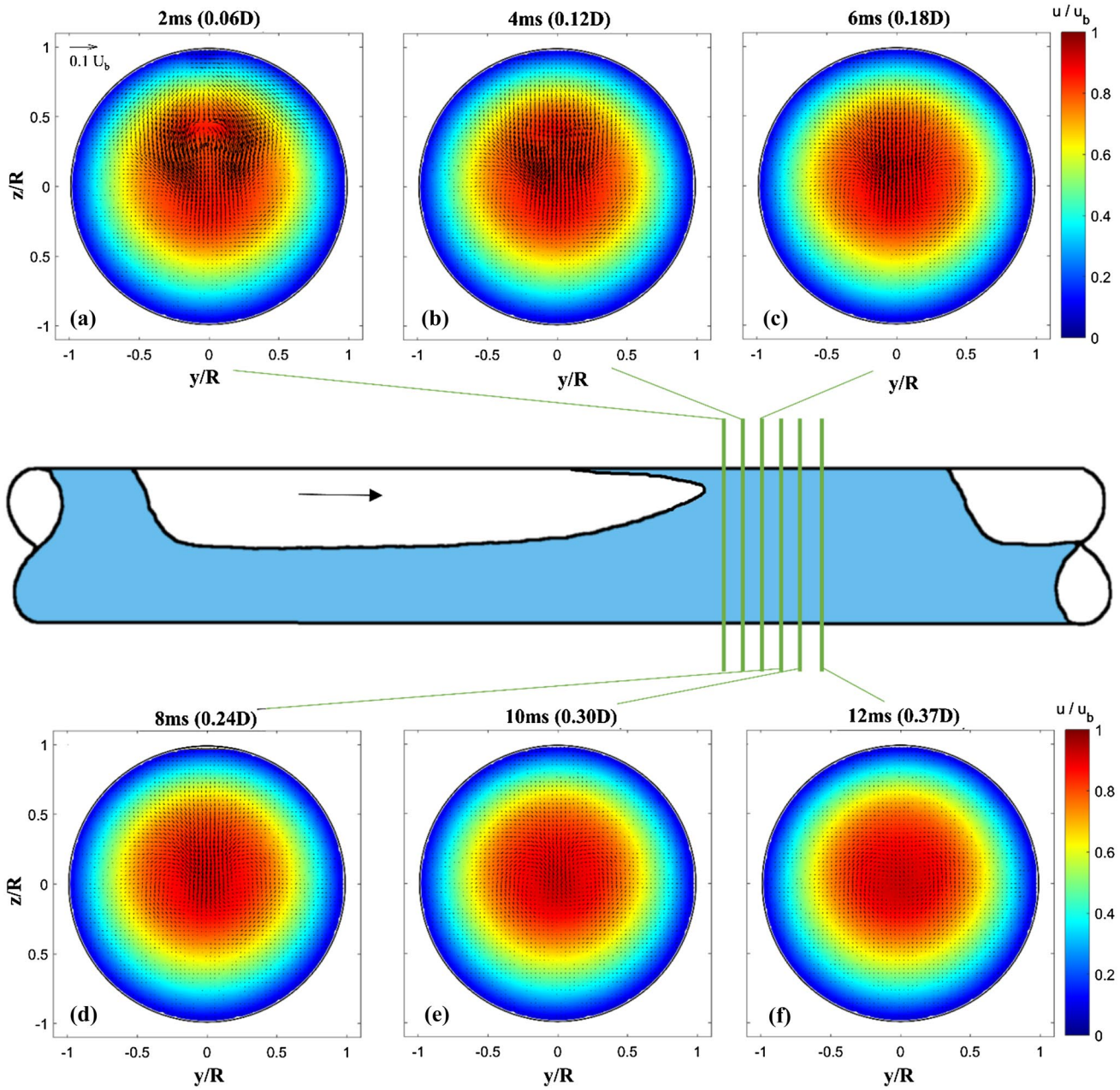


**Fig. 6** Three-component velocity fields in the liquid plug region for different times or downstream positions from the bubble nose. **a** 2 ms (0.06*D*), **b** 4 ms (0.12*D*), **c** 6 ms (0.18*D*), **d** 8 ms (0.24*D*), **e** 10 ms (0.30*D*), **f** 12 ms (0.37*D*)

section. As the streamwise distance from the bubble nose is increased, it can be noted in Fig. 6b–e that the intensity of the downward jet-like flow is progressively decreased, and that the cores of the streamwise vortices are progressively displaced toward the pipe centerline. At the furthest measured downstream position, 0.37*D* in Fig. 6e, the downward flow observed persisted and seem to be due solely to the pair of streamwise counter rotating vortices originated from the downward flow, which are now nearly at the pipe centerline.

Figure 7 presents streamwise velocity profiles extracted from the three component measurements just displayed in Fig. 6. These profiles were extracted from a vertical line crossing the pipe center. Again, the influence of the faster moving gas bubble on the liquid velocity profile is clearly observed. The velocity profile displays two inflection points with local maxima around $z/R = 0.4$ and $z/R = -0.25$ for the plane closest to the bubble nose, Fig. 7a. Similar observations were made in the work of Carneiro at al. (2011). The streamwise velocity profile is seen to tend to a symmetric

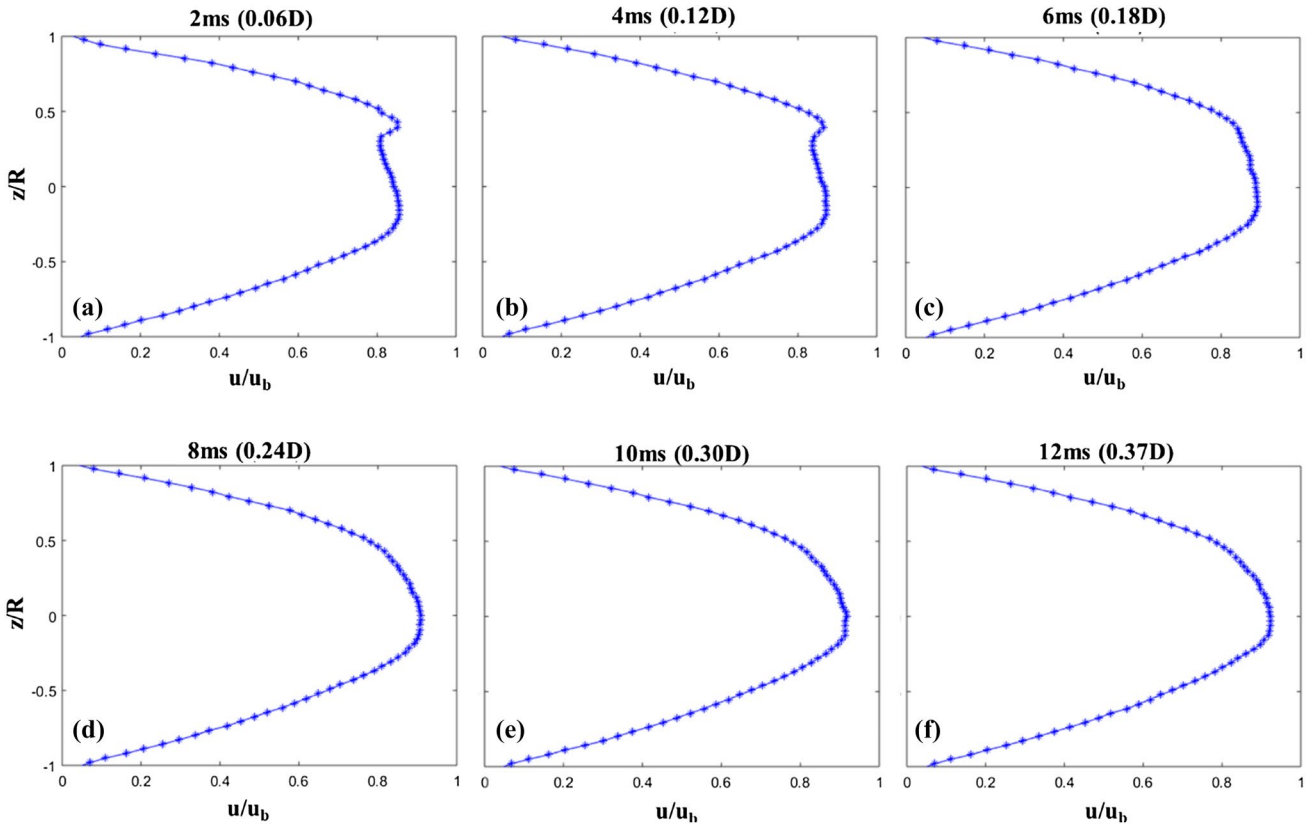


**Fig. 7** Streamwise velocity profiles in the liquid plug region for different times or downstream positions from the bubble nose: **a** 2 ms (0.06*D*), **b** 4 ms (0.12*D*), **c** 6 ms (0.18*D*), **d** 8 ms (0.24*D*), **e** 10 ms (0.30*D*), **f** 12 ms (0.37*D*)

parabolic profile for positions further downstream, but a fully-developed profile is not achieved within the liquid plug region, for the case investigated.

We now turn attention to the velocity profiles measured upstream of the bubble nose, within the liquid film region. Figure 8a–f present the measured results in a similar format as that employed in Fig. 6. As explained in Sect. 3.2, the white areas in the plots are the masked regions where velocity measurements could not be performed due to the obstruction of the camera views by the bubble. The black contour is the gas–liquid interface. The masked areas, as expected, are larger than the gas–liquid interface.

The velocity field measured closest to the bubble nose, upstream of its position, Fig. 8f, shows that the bubble passage imposes, both, and upward liquid flow above the bubble and a downward flow under the bubble. At this region, and for the conditions of the experiment, the bubble did not touch the upper or side parts of the pipe wall, leaving room for a recirculation motion in the space between the bubble and the top part of the pipe wall. The downward motion along the sides of the bubble seems to aid in the formation of the pair of symmetric counter rotating vortices that were detected in the liquid plug region. The same circular motion was observed in the simulations developed for an air–water mixture, by Febres at al. (2010). For velocity fields at planes further upstream into the liquid film, Fig. 8a–e, the region occupied by the bubble grows, what causes the intensity of the circular motion around the gas bubble to increases, since the side passage available for the liquid to flow between the gas bubble and the pipe wall becomes smaller, and this effect seem to overcome the increased friction in the narrower passages. At the furthest upstream axial position corresponding to Fig. 8a, the flow still presents strong three-dimensional components.

Streamwise velocity profiles at a vertical line crossing the center of the pipe are presented in Fig. 9, for different axial positions upstream of the bubble nose, where there is still liquid above the bubble. A general observation of the velocity profiles presented in the figure shows that the liquid streamwise velocity components above and below the bubble are slower than the bubble velocity, as can be verified by the magnitudes of the velocities made dimensionless by the bubble velocity. It is interesting to note that there is a decrease in the liquid velocity at the positions closest to the interface. It should be mentioned that this trend was also observed in the instantaneous velocity profiles that were used to compute the ensemble-averaged profiles presented in the figure.

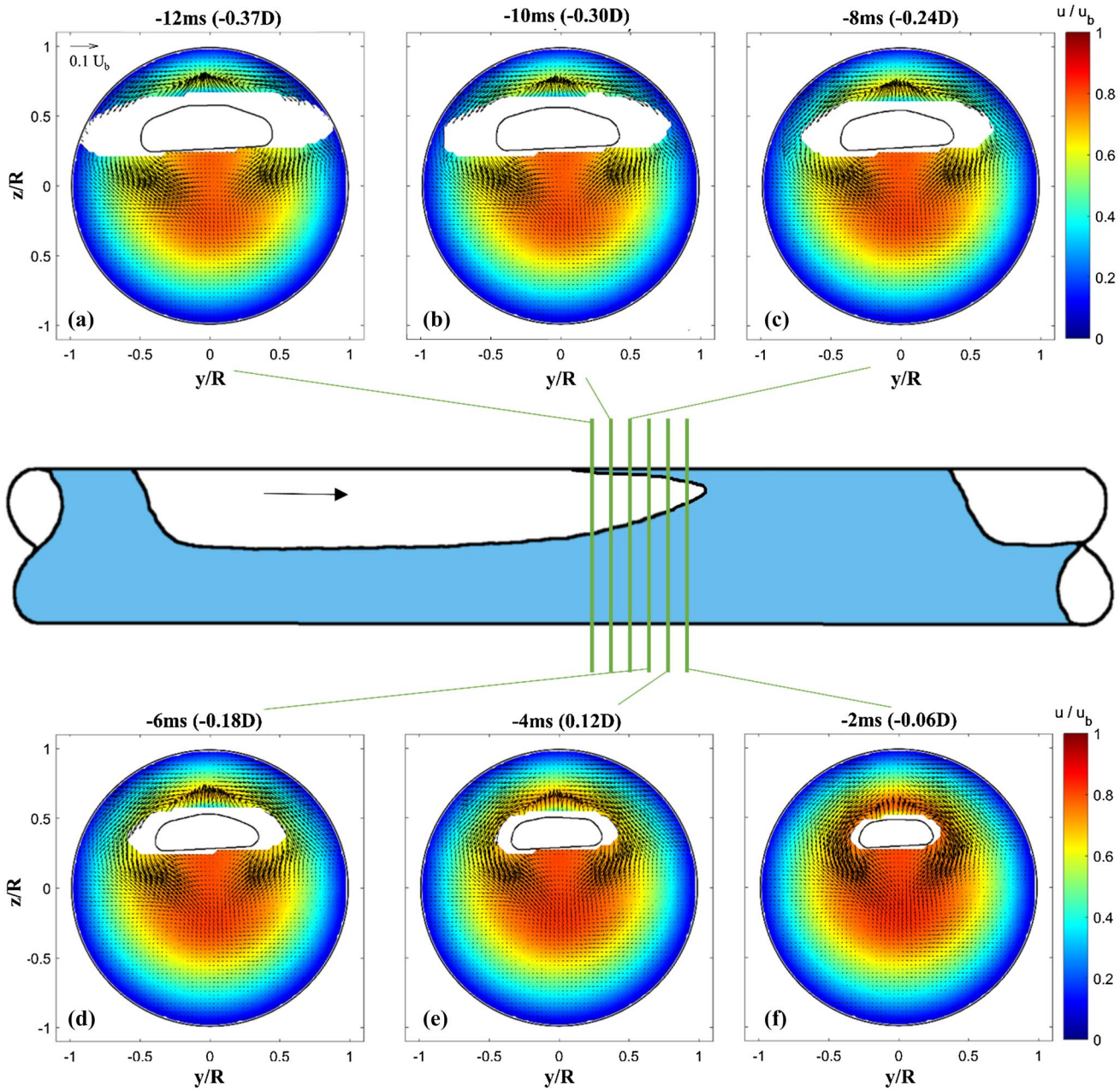


**Fig. 8** Three component velocity fields in the liquid film region for different times and upstream positions from the bubble nose: **a** −12 ms (−0.37*D*), **b** −10 ms (−0.30*D*), **c** −8 ms (−0.24*D*), **d** −6 ms (−0.18*D*), **e** −4 ms (−0.12*D*), **f** −2 ms (−0.06*D*). White areas in the figures represent the masked regions, where velocity measurements could not be performed. Black contours represent the gas–liquid interface

The decrease in the velocity value close to the interface can be rationalized by considering that the interface moves at a velocity that is different from the velocity of the bubble. The bubble velocity is a translation velocity representing the whole bubble, while the interface displays different velocities at different positions along its surface. In fact, for the same axial position, the upper part of the interface presents a velocity that is even smaller than the interface velocity at the lower part of the bubble. This it attributed to the fact that the narrower liquid space at the upper part of the bubble induces higher shear levels and, therefore, a higher deceleration of the interface. To be consistent with the physical requirement of equality of shear stresses at the interface from the gas and liquid sides, the gas velocity profiles within the bubble will display negative derivatives at the interface. Circulatory motions in the gas phase will be established to accommodate

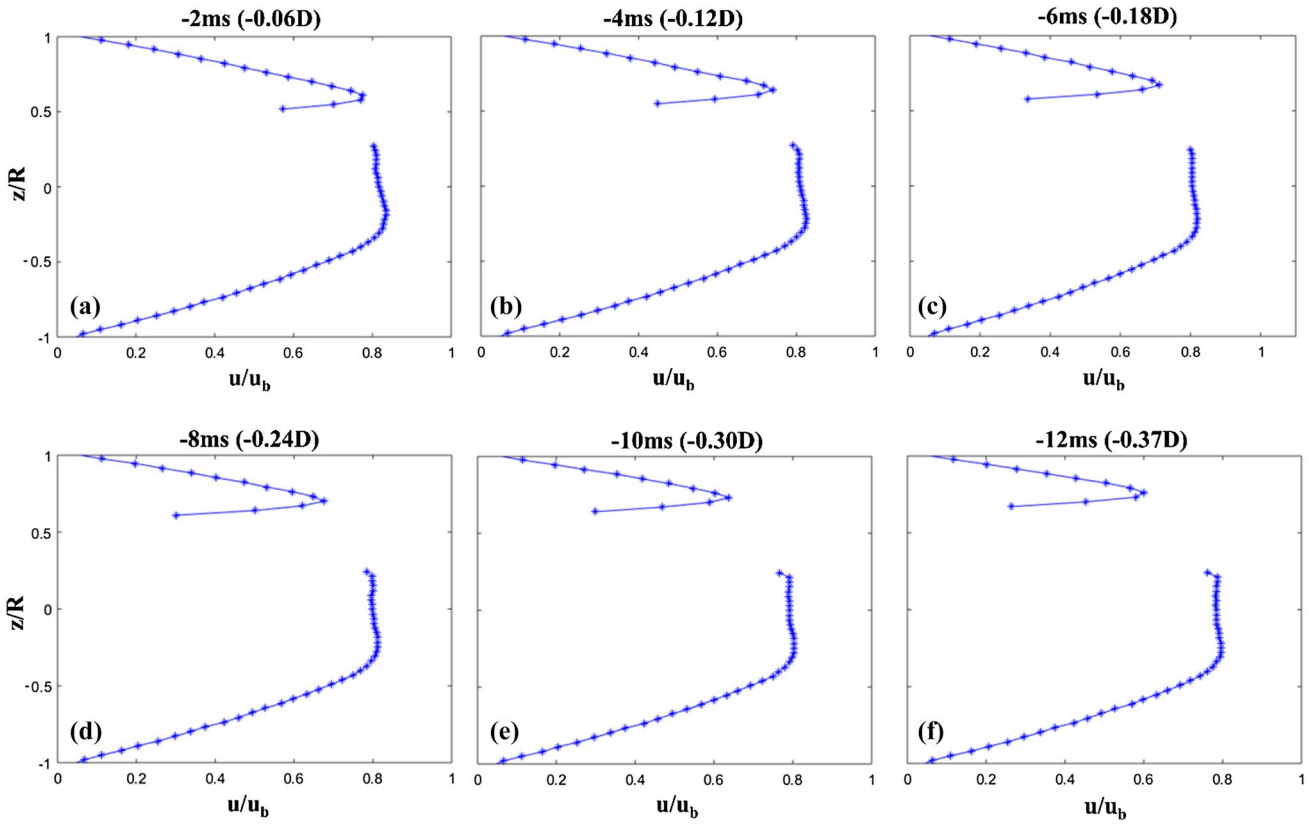


**Fig. 9** Streamwise velocity profiles in the liquid film region for different times or upstream positions from the bubble nose. **a** −2 ms (−0.06*D*), **b** −4 ms (−0.12*D*), **c** −6 ms (−0.18*D*), **d** −8 ms (−0.24*D*), **e** −10 ms (−0.30*D*), **f** −12 ms (−0.37*D*)

the motion of the interface and the matching of the shear stress at the interface. This circulatory motion, in the form of two counter-rotating recirculation regions, would be only visualized in the frame of reference of the bubble. In the laboratory frame of reference, the motion in the gas would be purely forward, although not uniform within the bubble. Siddiqui et al. (2016) performed planar PIV measurements in both the gas and liquid phases. Although with a somewhat limited spatial resolution, their results do demonstrate the presence of circulation zones in the gas phase, as conjectured above.

An animation was prepared combining the streamwise velocity profiles for the liquid plug and film regions presented in Figs. 7 and 9 and the three-component velocity fields presented in Figs. 6 and 8. In this movie the effect of the passage of the faster-moving nose bubble on the velocity profiles can be clearly seen. This movie can be found as Supplementary Material to the present paper. A few features of the flow revealed by the animation are interesting to be noted. The first liquid velocity profile presented is at a position 0.37*D* downstream of the incoming bubble nose. At this position, the liquid occupies the whole pipe cross section, and the velocity displays a nearly parabolic profile with its maximum a little above the pipe centerline. As the bubble is approaching the location of the measuring plane (position 0.12*D*), one can observe that the maximum of the velocity profile moves upward as a consequence of the oncoming faster-moving bubble nose, as already commented when presenting the results from Fig. 7. The liquid around the center line is decelerated due to the downwash produced by the oncoming bubble. When the bubble crosses the measuring plane (0.0*D*), the liquid profile splits in the upper and lower parts. It is interesting to note the immediate drop of the velocity close to the interface in both the upper and lower liquid profiles. As commented above, this drop is induced by the interface moving at a velocity that is smaller than the bubble velocity. The deceleration trend of the liquid profiles at the interface continues until the last measured profile at 0.37*D* upstream of the bubble nose.

Streamwise velocity profiles measured for positions further downstream into the liquid plug and upstream into the liquid film are presented in Fig. 10a, b, respectively. In Fig. 10a the profile at 0.06*D* already presented in Fig. 7 is plotted to serve as a reference. As can be seen in the figure, the streamwise velocity profiles are similar for the different downstream positions. Even for the profile at 6.1*D*, a fully developed condition was not achieved, as can be witnessed by the upward displacement of the point of maximum

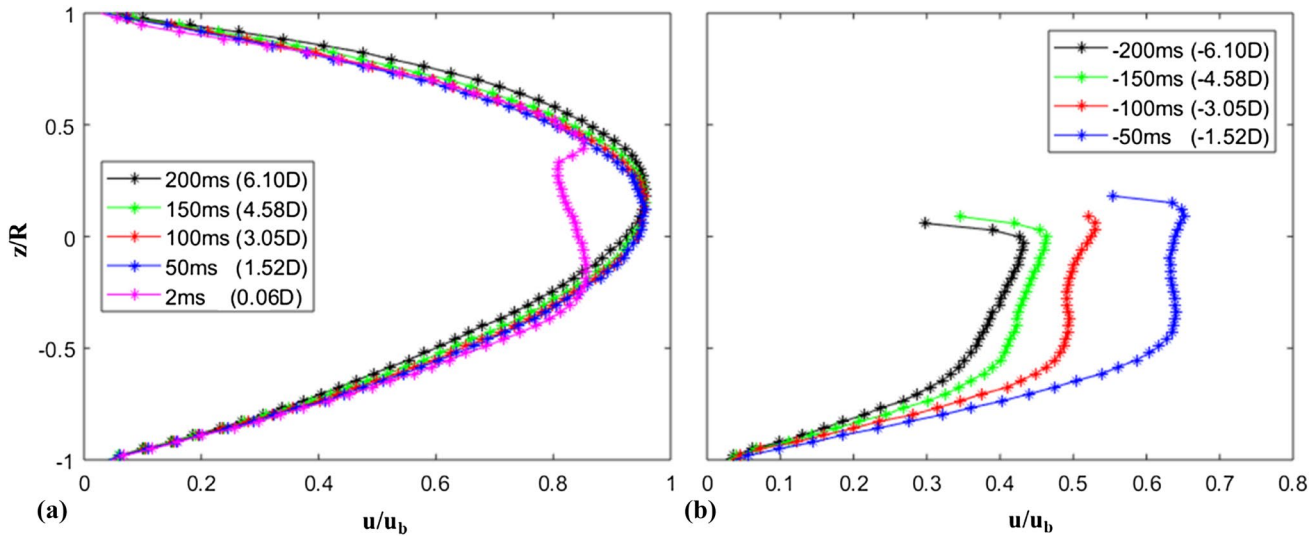


**Fig. 10** Normalized average streamwise velocity profiles at the pipe central plane at different positions: **a** downstream and **b** upstream of the elongated bubble nose

velocity from the pipe centerline. For the positions upstream into the liquid film region, Fig. 10b, an acceleration of the velocity for axial positions closer to the bubble nose is observed. This attributed to the effect of the bubble pushing the liquid forward, in the laboratory frame of reference. As already commented for the axial positions displayed in Fig. 9, a decrease in the velocity at transverse positions adjacent to the bubble interface is also observed for all axial positions presented in Fig. 10.

The SPIV technique employed allows the calculation of the magnitude of the streamwise component of the vorticity vector, $\omega_x$, in each investigated plane, downstream and upstream of the bubble nose. The vorticity was computed by a central difference scheme using the measured in-plane velocity components These results are presented in Fig. 11 for some selected streamwise positions upstream and downstream of the bubble nose. In the figure, the in-plane components of the velocity vector are also displayed as black arrows, while the magnitude of the streamwise vorticity component is color-coded to the scale to the right. The presence of the symmetric pair of counter rotating streamwise vortices aforementioned is clearly observed in the vorticity fields. For the downstream positions, the weakening of the vortices strength is verified for positions further downstream of the bubble nose, as already commented. For the upstream positions where the bubble is present, two pairs of symmetric vortices are observed, one on top of the other, indicating that a complex structure of vortices is formed around the bubble interface.

Since averaged velocity fields were available separated by a small time interval, it was possible to reconstruct the three-dimensional average velocity and vorticity fields around the elongated bubble nose. Figure 12 displays a picture of the ensemble-averaged structure of the gas bubble nose shape and the associated vortex system induced in the liquid surroundings. The red and blue isosurfaces represent the positive ($\omega_x = 8\ s^{-1}$) and negative ($\omega_x = -8\ s^{-1}$) magnitudes of the axial vorticity, while the yellow isosurface is the gas–liquid interface. The normal planes represent the magnitude of the streamwise component of the liquid velocity. As mentioned before, the three-dimensional representation clearly reveals the two long counter-rotating pairs of vortices, nested in the region below the elongated bubble, displaying a length greater than three pipe diameters, for the threshold value of $8\ s^{-1}$ employed. A smaller counter-rotating pair of vortices is also visible above the bubble, close to the bubble nose, representing the recirculating liquid found between the bubble nose and the upper part of the pipe wall.

## 7 Conclusions

The present work describes an experimental procedure developed to measure the instantaneous and ensemble-averaged, three-component velocity fields in the liquid region of a gas–liquid intermittent flow in a horizontal pipe. The procedure combined high-frequency stereoscopic particle image velocimetry (SPIV) and laser induced fluorescence (LIF) techniques. A set of photogates was used to trigger the SPIV system, allowing for the measurement of velocity fields in the liquid plug, downstream of the elongated bubble, and in the liquid film, upstream of the elongated bubble nose reference position.

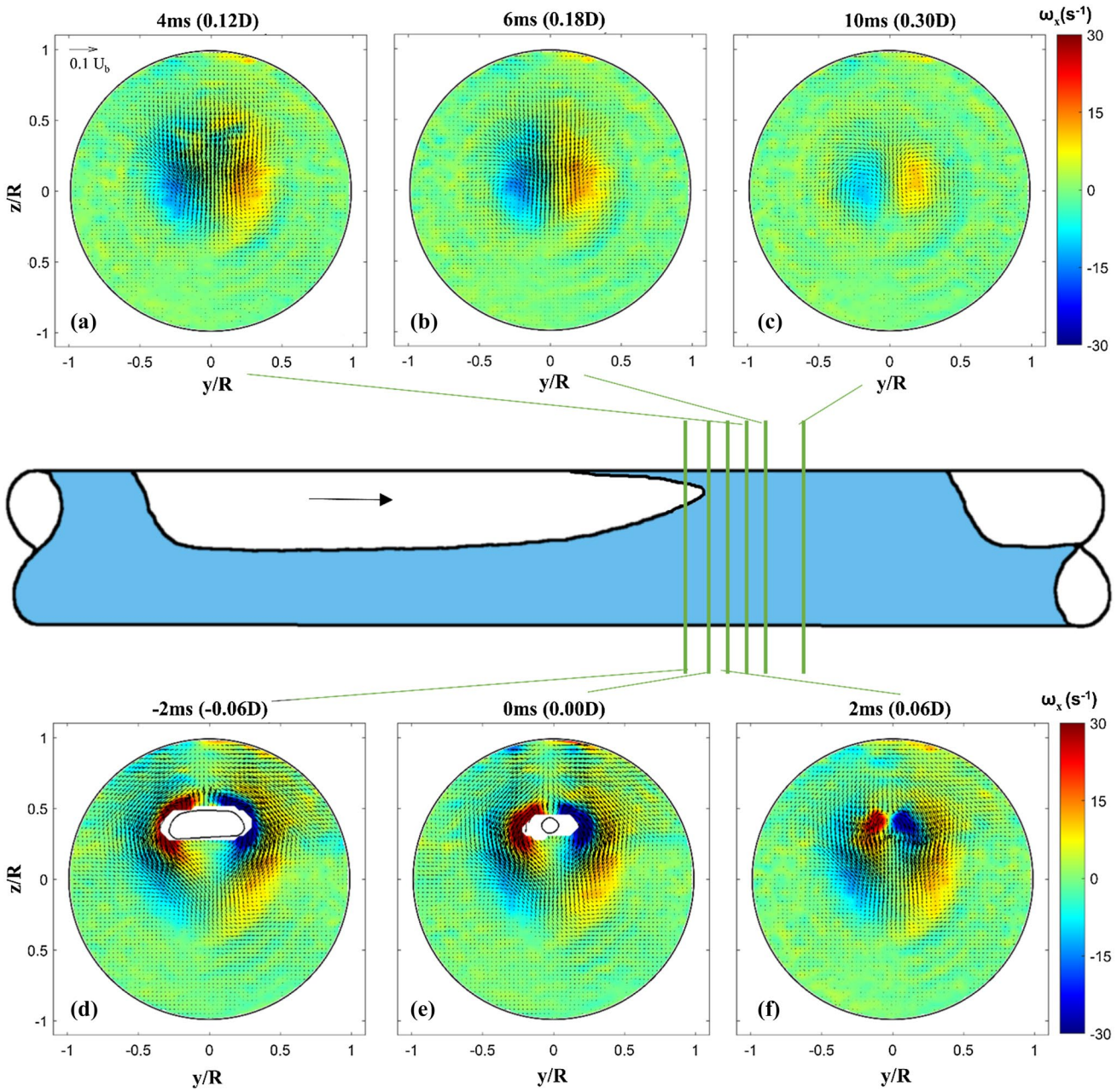


**Fig. 11** Magnitude of the axial component of the vorticity vector for different regions upstream and downsteam, close to the elongated bubble nose. **a** 4 ms (0.12*D*), **b** 6 ms (18*D*), **c** 10 ms (0.30*D*), **d** −2 ms (−0.06*D*), **e** 0 ms (0.00*D*), **f** 2 ms (0.06*D*). White areas in the figures represent the masked regions, where velocity measurements could not be performed. Black contours represent the gas–liquid interface

Image processing routines were developed to identify the cross section of the gas–liquid interface in each image frame. In addition, especial image processing routines were developed to identify and mask regions in the liquid flow in which the presence of the gas bubble did not allow the simultaneous views of the tracer particles from the two SPIV cameras, thereby precluding the velocity measurements.

The tests were conducted with a mixture of water and glycerine as the liquid phase, while air was used as the gas phase. The tests were conducted with superficial liquid and gas velocities of 0.4 m/s and 0.2 m/s, respectively, leading to a mixture Reynolds number of 493 and a mixture Froude number of 0.96, corresponding to the elongated bubble flow pattern.

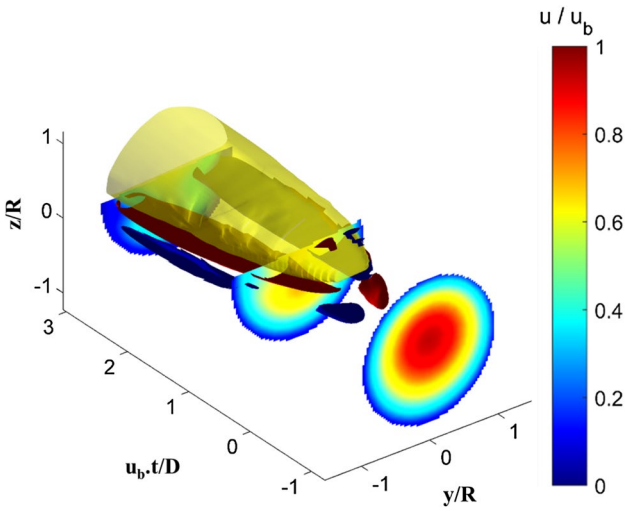


**Fig. 12** Three-dimensional reconstruction displaying the evolution of vortical coherent structures and average velocity field around the elongated bubble. Cross-sectional planes are color-coded by the normalized average streamwise velocity. Yellow isosurface represents the gas–liquid interface, while blue and red isosurfaces are the negative ($\omega_x = -8\ s^{-1}$) and positive ($\omega_x = 8\ s^{-1}$) axial vorticities, respectively

For each bubble passage event, 400 SPIV images were acquired at a 1 kHz rate. Ensemble-averaged information was obtained from 150 bubble passage events yielding well-converged, three-component velocity fields along the liquid plug and film regions. Although instantaneous SPIV measurements of elongated bubble two-phase flows are found in the literature, the present triggering system allowed, seemingly for the first time, the measurement of well-converged average three-component velocity field information. Typically, 3300 liquid velocity vectors were obtained for each cross section, leading to a fine spatial resolution of $0.6 \times 0.6$ mm. The photogate triggering system was also employed to measure the ensemble-averaged bubble velocity. This information was used to transform time-based information obtained from the SPIV system into space-based information.

The results for the velocity field in the liquid plug region showed the influence of the faster-moving gas bubble, inducing a downward jet, and two counter-rotating vortices for positions close to bubble nose. For positions in the liquid plug further downstream of the bubble nose, the jet-like flow was seen to attenuate, while the pair of vortices attained a centralized position in the pipe cross section. Streamwise velocity profiles in the liquid plug displayed the effect of the bubble presence, and did not attain a fully-developed hydrodynamic shape. Upstream of the bubble nose, complex recirculation patterns were captured in the liquid film under the bubble and in the space between the bubble and the pipe upper part. For positions further upstream of the bubble, only the liquid film under the bubble was observed, and the flow was seen to always display a three dimensional configuration with systems of counter-routing vortices superimposed on the axial flow.

The streamwise component of the vorticity vector in the plug and film regions were extracted from the measured velocity flow field. The visualization of the ensemble-averaged vorticity maps confirmed the flow structure configurations observed form the velocity fields.

The planar ensemble-averaged vorticity information was used to construct a three-dimensional representation of the ensemble-averaged structure of the gas bubble nose-region and the associated vortical structures induced in the liquid film and plug regions. The 3D visualization revealed the complex structure of the liquid flow.

The experimental procedure developed presented well-converged three-dimensional ensemble-averaged information on the structure of the liquid flow for an intermittent gas–liquid flow in the elongated flow pattern. The use of the procedure in flows where a higher number of dispersed bubbles are present, such as the slug flow pattern, is feasible, requiring, however, further improvement on the image processing procedures.

**Acknowledgements** The present work is part of an ongoing research project in two-phase flow carried in the Laboratory of Fluid Engineering, at PUC-Rio, in a partnership with Petrobras. The authors sincerely acknowledge the continuous support from Petrobras. Scholarship support by CAPES, agency from the Brazilian Ministry of Education, CNPq, Brazilian Research Council, and FAPERJ, Research Foundation of the State of Rio de Janeiro, is gratefully acknowledged.

## References

Ahmed WH (2011) Experimental investigation of air-oil slug flow using capacitance probes, hot-film anemometer, and image processing. Int J Multiph Flow 37:876–887

Baker O (1954) Design of pipelines for simultaneous flow of oil and gas. Oil Gas J 53:185–195

Bertola V (2002) Slug velocity in horizontal gas-liquid flow. Experiments in Fluids Vol 22:722–727

BIPM, IEC, IFCC, ILAC, ISO IUPAC, IUPAP, OIML (2008) Evaluation of measurement data—guide to the expression of uncertainty in measurement. JCGM 100:2008

Bjorkquist DC (2002) Stereo PIV calibration verification. In: 11th international symposium on applications of laser techniques to fluid mechanics, Lisbon, Portugal, 8–11 July

Carneiro J, Fonseca R Jr, Ortega A, Chucuya R, Nieckele A, Azevedo LFA (2011) Statistical characterization of two-phase slug ow in a horizontal pipe. J Braz Soc Mech Sci Eng 33:251–258

Carpintero-Rogero E (2008) Experimental investigation of transient slug flow. PhD Thesis, Technische Universitat Munchen

Czapp M, Muller C, Fernández PA, Sattelmayer T (2012) High-speed Stereo and 2D PIV measurements of two-phase slug flow in a horizontal pipe. In: 16th international symposium on applications of laser techniques to fluid mechanics, Lisbon, Portugal, 9–12 July

De Oliveira WR, de Paula IB, Martins FJWA, Farias PSC, Azevedo LFA (2015) Bubble characterization in horizontal air-water intermittent flow. Int J Multiph Flow 69:18–30

Dukler AE, Hubbard MG (1975) A model for gas-liquid slug flow in horizontal and near horizontal tubes. Ind Eng Chem Fundam 14(4):337–347

Fabre J (1994) Advancements of two-phase slug flow modeling. The University centennial petroleum engineering symposium SPE paper 27961-MS

Fabre J, Peresson LL, Corteville J, Odello R, Bourgeois T (1990) Severe sluggingin pipeline/riser systems. SPE Prod Eng 5(3):299–305

Farias PSC, Martins FJWA, Sampaio LEB, Serfaty R, Azevedo LFA (2012) Liquid film characterization in horizontal, annular, two-phase, gas-liquid flow using time-resolved laser-induced fluorescence. Exp Fluids 52(3):633–645

Febres M, Nieckele A, Fonseca R Jr, Azevedo LFA (2010) Three-dimensional unit slug in a horizontal pipe. In: 7th international conference on multiphase flow, Tampa, 30 May–4 June

Goharzadeh A, Rodgers P (2009) Experimental characterization of slug flow velocity distribution in two phase pipe flow. In: ASME 2009 international mechanical engineering congress and exposition. American Society of Mechanical Engineers, Lake Buena Vista, Florida, November 13–19

Kim TW, Aydin TB, Pereyra E, Sarica C (2018) Detailed flow field measurements and analysis in highly viscous slug flow in horizontal pipes. Int J Multiph Flow 106:75–94

Kvernvold O, Vindoy V, Sontvedt T, Saasen A, Selmer-Olsen S (1984) Velocity distribution in horizontal slug flow. Int J Multiph Flow 10:447–457

Lewis S, Fu WL, Kajasoy G (2002) Internal flow structure description of slug flow pattern in a horizontal pipe. Int J Heat Mass Transfer 45:3897–3910

Lindken R, Merzkirch W (2002) A novel technique for measurements in multiphase flow and its application to two-phase bubbly flows. Exp Fluids 33:814–825

Prasad AK (2000) Stereoscopic particle image velocimetry. Exp Fluids 29:103–116

Raffel M, Willert CE, Scarano F, Kähler CJ, Wereley ST, Kompenhans J (2018) Particle image velocimetry: a practical guide. Springer, New York

Sciacchitano A, Wieneke B (2016) PIV uncertainty propagation. Meas Sci Technol 27(8):084006

Sharma S, Lewis S, Kojasoy G (1998) Local studies in horizontal gas-liquid slug flow. Nucl Eng Des 184:305–318

Siddiqui MI, Muni S, Heikal MR, de Sercey G, Rashid A, Aziz A, Dass SC (2016) Simultaneous velocity measurements and the coupling effect of liquid and gas phases in slug flow using PIV-LIF technique. J Vis 19:103–114

Soloff SM, Adrian RJ, Liu Z-C (1997) Distortion compensation for generalized stereoscopic particle image velocimetry. Meas Sci Technol 8(12):1441–1454

Suzanne C, Ellingsen K, Risso F, Roid V (1998) Local measurements in turbulent bubbly flows. Nucl Eng Des 184:319–327

Wieneke B (2005) Stereo-PIV using self-calibration on particle images. Exp Fluids 39(2):267–280